Synthesis and Characterization of RuS_2 Nanostructures

David Díaz,*,† Silvia E. Castillo-Blum,† Octavio Álvarez-Fregoso,‡ Geonel Rodríguez-Gattorno,†,|| Patricia Santiago-Jacinto,§ Luis Rendon,§ Luis Ortiz-Frade,† and Yolia-Judith León-Paredes†

Facultad de Química, Instituto de Investigación en Materiales, and Instituto de Física, Universidad Nacional Autónoma de México, Coyoacán, 04510, México D.F., México

Received: August 18, 2005; In Final Form: October 10, 2005

Small naked ruthenium sulfide nanoparticles (NPs) with narrow size distribution (2.5 ± 0.4 nm of diameter) were synthesized in DMSO colloidal dispersions, under mild reaction conditions and using commercial $RuCl_3$ as precursor. To test the chemical reactivity with soft and hard bases, fresh presynthesized RuS_2 colloids were mixed with triethylamine ($N(Et)_3$) and ammonium tetrathiomolybdate ($(NH_4)_2MoS_4$) dimethyl sulfoxide solutions. Naked $N(Et)_3$ and $[MoS_4]^{2-}$-capped RuS_2 nanoparticle colloids were characterized using UV−visible electronic absorption and emission spectroscopies and high-resolution transmission electron microscopy (HR-TEM). It has also been shown that capped RuS_2−$[MoS_4]^{2-}$ nanoparticles yield MoO_3 crystalline matrix by means of HR-TEM experiments. The emission spectra of RuS_2 and $N(Et)_3$−RuS_2 dispersions show that both nanosized materials have strong fluorescence. The existence of the ruthenium precursor species in solution was established by cyclic voltammetry. Moreover, naked RuS_2 NPs were mixed with a chemical mixture with composition similar to gasoline (dibenzothiophene (Bz_2S, 400 ppm), hexane, and toluene (55:45% v/v)). The reaction mixture consisted of two phases; in the polar phase, we found evidences of a strong interaction of Bz_2S and toluene with the naked RuS_2 NPs. We have also obtained self-organized thin films of capped $N(Et)_3$− and RuS_2−$[MoS_4]^{2-}$ nanoparticles. In both cases, the shape and thickness of the resulting thin films were controlled by a dynamic vacuum procedure. The thin films have been characterized by atomic force microscopy, scanning electron microscopy, HR-TEM, energy dispersion spectroscoy, X-ray diffraction, and absorbance and fluorescence spectroscopies.

Introduction

RuS_2 is an interesting example of a pyrite-type structure material (isomorphous to FeS_2) of space group *Pa*3.[1] Optical absorption, resonance Raman scattering, and Raman scattering measurements of RuS_2 single crystals had been achieved.[2] Likewise, the surface structure of semiconductor RuS_2 has been investigated by low-energy electron diffraction and scanning tunneling microscopy.[3] Cubic-phase macrocrystals of RuS_2 show ability to lose an important amount of sulfur without changing their morphological and structural properties. Despite its technological importance, there has been considerable controversy about the reported energy band gap values for RuS_2 (E_g = 1.22−1.85 eV).[4] It is considered as a narrow-energy band-gap semiconductor with energy bands derived from Ru d states.[5] Besides, a summary and estimates of thermodynamic properties for ruthenium, rhodium, palladium, and platinum solids, aqueous ions, and complexes appeared in 1998.[6]

Ruthenium sulfide has been traditionally considered as a Ru(IV) species;[7] however, R. R. Chianelli et al. reported that both poorly and well-crystallized RuS_2 samples are diamagnetic species. Ru(II) is the only species showing this magnetic behavior; therefore disulfide ions are coordinated to the metal ion in ruthenium sulfide.[8] M. Breysse and collaborators have reported the characterization of silica-supported RuS_2 using the methyl mercaptan condensation reaction as a test reaction.[9] The high stability of RuS_2 against hydrogen and oxygen evolution from aqueous solution makes RuS_2 nanoparticles interesting to use for the photoelectrolysis of water with visible light. Upon illumination, photogenerated valence-band holes are transferred to the Ru surface states where oxidation of water to molecular oxygen takes place via an interfacial coordination reaction.[10] Also, RuS_2 exhibits prominent hydrogenation properties.[11] B. J. Tatarchuk and co-workers used neutron-scattering spectroscopy to determine hydrogen adsorption sites on ruthenium sulfide at 300 K.[12] H. Jobic et al. have claimed the identification of new hydrogen species adsorbed onto RuS_2 by inelastic neutron-scattering spectroscopy.[13] As catalytic species, ruthenium sulfide is one of the most active chalcogenide, 13 times more active than molybdenum sulfide in the hydrodesulfurization of thiophene and 10 times in the hydrogenation of biphenyl.[14] Moreover, some electronic structure studies had been performed.[15,16] Hitherto, we had found few published studies concerning RuS_2 nanoparticles.[17] It is important to point out that the reported synthesis pathways of the RuS_2 nanoparticles take place under high-vacuum or high-temperature reaction conditions.

Regardless of the chemical and technological importance of RuS_2, the theoretical and experimental understanding of the variation of the physical and chemical properties depending on particle size is still incomplete. RuS_2 colloidal dispersions had

* To whom correspondence should be addressed. Phone: +52-55-56223813. Fax: +52-55-56223813. E-mail: david@servidor.unam.mx.

† Facultad de Química, Universidad Nacional Autónoma de México.

‡ Instituto de Investigación en Materiales, Universidad Nacional Autónoma de México.

§ Instituto de Física, Universidad Nacional Autónoma de México.

|| Present address: Instituto Mexicano del Petróleo, Parque Ind. La Reforma, Km 7.5, CP 42083, Pachuca, Hidalgo, México.

10.1021/jp054669+ CCC: $30.25
Published on Web 11/08/2005

not been characterized, and neither had their optical properties been studied. Thin films of RuS_2 nanoparticles had not previously been obtained. Although good structural studies of RuS_2 nanocrystalls by high-resolution transmission electron microscopy (HR-TEM) had been performed, their characterization by high-angle annular dark field (HAADF) and electron energy loss spectroscopy (EELS) studies had not been carried out.

Here we report a novel and simple synthetic method and an extensive characterization of stable colloidal dispersions and thin films of naked and capped RuS_2 nanoparticles. The optical properties of RuS_2 colloidal dispersions are extensively discussed. A detailed HR-TEM study of size and shape of nanocrystallites was performed. This is the first report, to our knowledge, of a detailed study and discussion of the absorption and emission spectra of RuS_2 colloidal dispersions. In addition, we carried out a careful electrochemical study of the precursor ruthenium species in solution. Besides, we have synthesized surface-modified nanoparticles of ruthenium sulfide capped with inorganic and organic Lewis bases. Additionally, the interaction of RuS_2 NPs with a mixture with composition similar to gasoline was investigated. Finally, we have collected experimental evidence of the presence of an ordered MoO_3 matrix, originated from the $RuS_2-[MoS_4]^{2-}$ colloidal dispersions, under normal reaction conditions.

Experimental Section

The chemical reagents were purchased as indicated: DMSO (99.9% high-performance liquid chromatography (HPLC) grade, Aldrich) $N(Et)_3$ (99%, Aldrich), and *commercial* $RuCl_3\ xH_2O$ (43.93% of ruthenium, Aldrich), ultra puris $Na_2S{\cdot}9H_2O$ from Fluka, stored at 4 °C. It is important to state that the oxidation number of ruthenium in this salt is mainly III; this is a mixture of chloro and chlorohydroxo species, and its surface consists mainly of Ru(IV). The initial surface composition of commercial $RuCl_3$ is assumed to be close to $Ru^{(III+x+y)}Cl_{3+y}(H_2O)_{3-x-y}(OH)_x$, resulting from the surface reaction between atmospheric water and $RuCl_3{\cdot}nH_2O$.[18] It is worth mentioning that the purity of Na_2S is an important factor for generating ultra small and narrow size-distribution nanoparticles. Ammonium tetrathiomolybdate (99%, Strem). Prepurified argon gas (99.998%, Praxair). 200-μm mesh amorphous carbon coated copper grids, fused quartz, (111) monocrystalline silicon wafers (from Monsanto), and Corning 7059 glass slides. Ultrapure water (8Ω, obtained from an Easypure compact Ultra, Barnstead, deionization system). UV−visible electronic absorption spectra were collected from an 8452A-diode array Hewlett-Packard spectrophotometer coupled to a temperature-control Peltier system. Otherwise, the UV−visible fluorescence spectra were recorded in a Fluoromax-SPEX spectrophotometer at room temperature.

Preparation of Ruthenium Sulfide Colloidal Dispersions. The following is a description of a typical procedure to prepare 25 mL of RuS_2 particles. Commercial $RuCl_3$ (0.0016 g) was dissolved in 24.9 mL of DMSO, and then it was stirred until a transparent and dark amber solution was obtained. This was stirred overnight, at room temperature, until its color changed to bright green. Then, 0.5425 g of $Na_2S{\cdot}9H_2O$ was dissolved in 25 mL of Nanopure water under dynamic magnetic stirring. Then, argon was bubbled through this solution for 30 min, which was also vigorously stirred. An aliquot of 0.1 mL of sodium sulfide was pipetted off, and immediately dropped at once, under dynamic stirring, into the green ruthenium chloride DMSO solution that was covered by a moderate flow of Ar. The fresh colloid dispersion was stored under darkness, at room temperature, Figure 1 (curve c, part A), an immediate change is

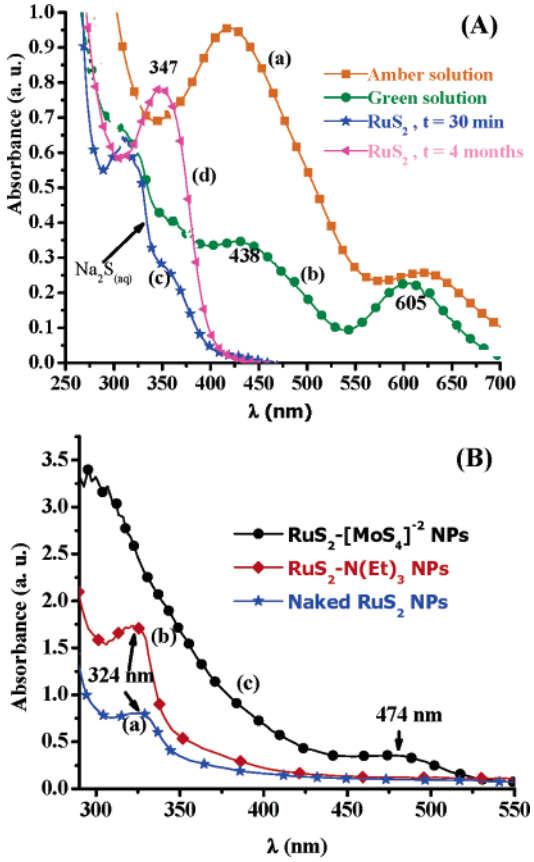

Figure 1. (A) Spectral changes of (a) 2×10^{-4} M commercial $RuCl_3$ DMSO solution, (b) 2×10^{-4} M commercial $RuCl_3$ DMSO solution, after 12 h, (c) 2×10^{-4} M commercial $RuCl_3$ DMSO solution after mixing with aqueous Na_2S, (d) RuS_2 NPs after 4 months of preparation. (B) (a) RuS_2 naked NPs in DMSO, (b) freshly prepared triethylamine capped RuS_2 NPs, (c) and freshly prepared tetrathiomolybdate capped RuS_2 NPs. These dispersions were prepared as described above.

observed on the electronic absorption spectrum profile. After four months, the colorless RuS_2 colloidal dispersion shows the typical electronic absorption spectrum in the ultraviolet region, with an absorption maximum at 347 nm as shown in Figure 1 (curve d, part A). The ripening process continues up to four months after the colloids preparation. These dispersions are stable at least for a year.

To synthesize capped nanoparticles, fresh 1×10^{-3} and 1.4×10^{-3} M DMSO solutions of $(NH_4)_2MoS_4$ and $N(Et)_3$, respectively,[19] were prepared. In each case, appropriate aliquots of the capping agents were mixed with an equal volume of the RuS_2 dispersion, always under vigorous stirring. The final stoichiometric ratios of the reaction mixtures were Ru:Mo 1:10 and Ru:N 1:14, respectively; this means that there is a large excess of both capping agents to ensure total cover of the surface NPs. Both capped nanoparticle dispersions were kept under darkness, at room temperature. These colloidal dispersions are also very stable at least during one year, Figure 1B. The addition of $N(Et)_3$ to the colloids caused an increase in the absorption but no shift of the position of the maximum absorbance; while the addition of tetrathiomolydate led to a bathochromic effect and decreased the absorption intensity; it was observed 2 days after mixing. The batochromic effect is caused by the influence of substitution or a change in environment.

Thin Films. Self-organized thin films of capped $N(Et)_3$ and $RuS_2-[MoS_4]^{2-}$ nanoparticles were obtained. In both cases, the shape and thickness of the films were controlled by a dynamic vacuum procedure, to slowly extract the solvent, using a Cook

SCHEME 1

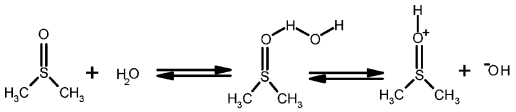

(I)

$$2\,S^{2-}_{(aq)} \xrightarrow[O_2]{[OH]^-} [S_2]^{2-}_{(aq)} + 2e^- \quad \text{(II)}$$

$$2\,Ru^{+3}_{(DMSO)} + 2e^- \longrightarrow 2\,Ru^{+2}_{(DMSO)} \quad \text{(III)}$$

$$Ru^{+2}_{(DMSO)} + [S_2]^{-2}_{(solv)} \longrightarrow RuS_2 \quad \text{(IV)}$$

$$Ru^{+4}_{(DMSO)} + 2e^- \longrightarrow Ru^{+2}_{(DMSO)} \quad \text{(V)}$$

Vacuum Mag 3 magnetron sputtering. In this case, Argon Infra Ultrapure 99.9999% was used as transport gas.

The X-ray diffraction patterns were recorded on a Siemens, D5000, powder diffractometer, with a graphite monochromator. In this case, the experimental conditions were 20 mA and 40 kV, using a copper anode and nickel filter for $\lambda = 1.5444$ Å. Energy-dispersion spectra and scanning electron photographs were acquired from a SE microscope (Leica-Cambridge 440, Stereoscan), coupled to an energy-dispersive analyzer (Pentafet-Oxford). Whereas atomic force microscopy (AFM) images were obtained in an AF Park Scientific Instruments, 1.0-C. P. microscope. The HR-TEM, HAADF, and EELS studies were performed in a JEM 2010 microscope with a Gatan Image Filter (GIF) attached to the system. The microscope is also equipped with bright-field and HAADF detectors. The conventional HR-TEM images were obtained in Scherzer condition.

Electrochemical Studies. All electrochemical measurements were performed in DMSO solutions containing tetra-*N*-butylammonium tetrafluoroborate ($TBABF_4$, 0.1 M, 99% Aldrich) as supporting electrolyte. An EG&G PARC model 263-A potentiostat/galvanostat controlled by PC software was used. A typical three-electrode array was employed for all electrochemical measurements: platinum disk as working electrode, platinum wire as counterelectrode, and a pseudoreference electrode of silver wire immersed in DMSO solutions with tetra-*N*-butylammonium chloride (TBACl, 0.1 M, 99% Fluka). All solutions were bubbled with nitrogen prior to each measurement. Voltammograms were initiated from open circuit potential (E_{ocp}), and the scan potential was obtained in the positive direction, the scan rate used was 100 mV s^{-1}. For these electrochemical experiments, 1×10^{-3} M $RuCl_3 \cdot 1.5H_2O$ in DMSO was employed taking in account the threshold detection of cyclic voltamperometry. The chloride standard calibration curve was obtained from solutions 1.0×10^{-3} to 4×10^{-3} M TBACl; the current was measured at anodic peak potential E_{pa}.

The starting materials and the solvents were used as received, without any further purification.

Results and Discussion

Synthetic Pathway. RuS_2 NPs have been prepared through different routes, utilizing thermal methods, in reverse micelles and heating under ultrahigh vacuum conditions.[17c,e,20,21,] We have chosen commercial $RuCl_3$ as the ruthenium source, an inexpensive material. As was stated in the Experimental Section, this material is the product of the partial hydrolysis of ruthenium trichloride, it contains Ru(III) and significant amounts of Ru(IV). In Scheme 1, we present a suggested synthetic route for RuS_2 colloidal NPs with the following sequence of reactions:

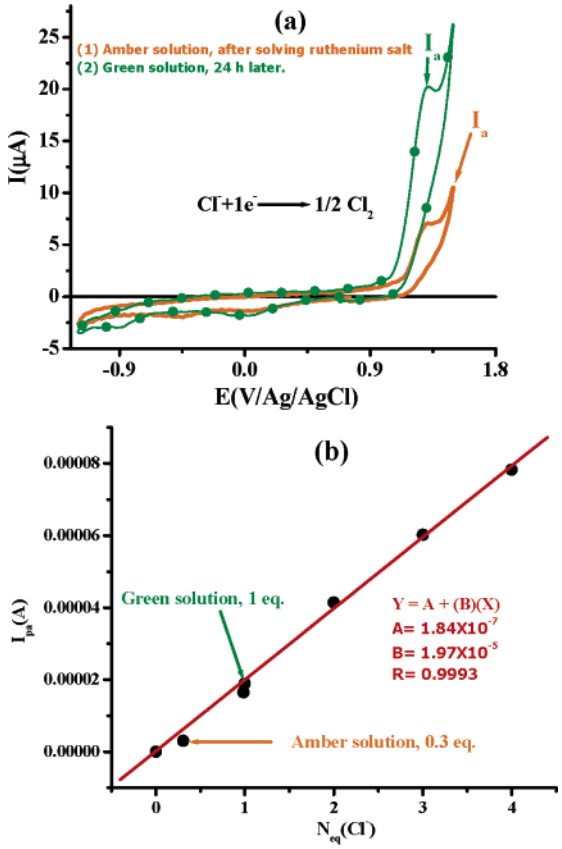

Figure 2. (a) Cyclic voltammograms of 1×10^{-3} M $RuCl_3 \cdot 1.5H_2O$ in the presence of 0.1 M $TBABF_4$ in DMSO. The scan was initiated from E_{ocp} in the positive direction. The scan rate was 100 mV s^{-1} with a Pt electrode. (1) Fresh solution and (2) 24 h later. (b) I_{pa} (A) vs N_{eq} (Cl^-) calibration curve corresponding to the oxidation of Cl^- from TBACl in the presence of 0.1 M $TBABF_4$ in DMSO. The scan rate was 100 mV s^{-1} with a Pt electrode.

Equation I shows the great affinity of water toward DMSO.[22] It is well known that DMSO is miscible in water in all proportions. Also, DMSO is classified as a polar, aprotic, and basic solvent.[23] We can find in such solutions a fair amount of hydroxyl anions. Besides, the solubility of molecular oxygen in DMSO is higher than in water, at room temperature. Therefore, in this reaction system the necessary components for the well-known thiol (sulfide) autoxidation reaction[24] are present, the reaction that takes place is illustrated in eq II. As a result of the disulfide species formation, there are enough electrons to reduce both Ru(III) and Ru(IV), eqs III and IV. Finally, Ru(II) and disulfide species can meet to produce RuS_2 NPs, eq V. This is a clean and direct synthetic process, and all these reactions are carried out at room temperature. The resulting RuS_2 dispersions are liophilic colloids since DMSO molecules are able to bind to the NP surface through multiple association−dissociation equilibria.

Ruthenium Precursor Species. To determine the chemical nature of the precursor (amber and green) solutions, see Figure 1 (curves a and b of part A), we decided to carry on electrochemical experiments, Figure 2. We found that after dissolving the ruthenium salt in DMSO one-third of a Cl^- chemical equivalent is released from the ruthenium coordination sphere. Twenty-four h later, 1 equiv of this ion was released, as shown in Scheme 2.

Under these reaction conditions, it was not possible to detect the reduction of ruthenium(III) or (IV) to Ru(II) by DMSO, since their reduction potentials are outside the electroactivity

SCHEME 2

$$RuCl_3 \cdot 1.5H_2O \xrightarrow[\text{After solving}]{\text{DMSO}} 0.3\,[RuCl_2(DMSO)_4]^{+1\text{ or }+2} + 0.3\,Cl^{-1} \quad 0.6\,[RuCl_3(DMSO)_3]^{0\text{ or }+1} \qquad \textbf{(I)}$$

$$\xrightarrow[\text{After 24 h.}]{} [RuCl_2(DMSO)_4]^{+1\text{ or }+2} + Cl^{-1} \qquad \textbf{(II)}$$

domain of the solvent. Scheme 2 shows the Cl^--releasing process.

From these results we suggest that the amber solution is a mixture of the solvated complex species $[RuCl_2(DMSO)_4]^{+1}$ or $^{+2}$ and $[RuCl_3(DMSO)_3]^{0}$ or $^{+1}$, taking into account that Ru(IV) is present on the surface of the salt. After 1 day, we recorded the presence of 1 Cl^- equiv, as illustrated in eq II. Hence the green solution is only constituted by $[RuCl_2(DMSO)_4]^{+1}$ or $^{+2}$ (Ru(III) and Ru(IV) species). This reaction scheme is consistent with the reaction sequence shown in the simplified Scheme 1. Obviously, we are avoiding including a discussion about the stability of the different possible isomers since the trans and mer isomers are the most stable, for the dichloro and trichloro complex species, respectively.

Optical Properties. The band-gap energy of RuS_2 NPs was estimated from the absorption edge value (obtained from the intersection of the tangent with the wavelength axis). Because of size quantum effects, the first excitonic transition (or band gap) increases in energy as the particle diameter decreases.[25]

As previously shown by the electronic absorption spectra in Figure 1, the naked RuS_2 NPs have a narrow size distribution, with a rather small size, and band-gap energy of 3.6 eV. The addition of capping agents shows two different effects: $N(Et)_3$ yields the same profile spectrum with higher absorbance. This result can be explained by the bonding of the amine to the Ru(II) dangling bonds, the free lone-electron pair from the amine occupies the ruthenium e_g orbitals (at surface states), hence increasing the number of electrons able to induce transitions, Figure 3. While with the tetrathiomolybdate anion, the red-shift absorption could be due to an increase of effective particle size ($(DMSO)_n-RuS_{2-}$ $[MoS_4]^{2-}{}_m$ particles). It is also observed that the spectrum profile completely changed in comparison with that of RuS_2 NPs, Figure 1 (curve c of part B). There is important absorption from 280 to 500 nm, which means that there are different sized chromophoric species, $[MoS_4]^{2-}$-capped NPs and free $[MoS_4]^{2-}$ anions due to the excess of this reagent. This may be due to the fact that the capping process with this Lewis base is rather slow and that excess $[MoS_4]^{2-}$ completely covers the surfaces. It is important to consider several factors when the affinity of RuS_2 toward $N(Et)_3$ is compared with that to $[MoS_4]^{2-}$, such as the charge of the base and stereoselectivity of the interaction.

The fluorescence spectra of the naked and $N(Et)_3$-capped RuS_2 colloids irradiated at 320 nm are shown in Figure 4. Both colloids have spectra of similar profiles, with the maximum at 380 nm. The width of the bands is of 200 nm, the exitonic peak appearing at 330 nm and also two shoulders can be observed at 365 and 410 nm, respectively. The capped NPs show 28 times higher emission than the naked NPs. Meanwhile, the $[MoS_4]^{-2}$ anions quench the RuS_2 NPs emission completely.

The intensity difference of the spectra can be explained in the following manner. For the naked NPs, the emission comes from the normal transitions of the electrons from the conduction to the valence band, with the participation of a considerable number of surface states, while for the capped NPs, there are additional injection of electrons from the amine ligands, occupying the d orbitals of the Ru(II) surface. It is worth

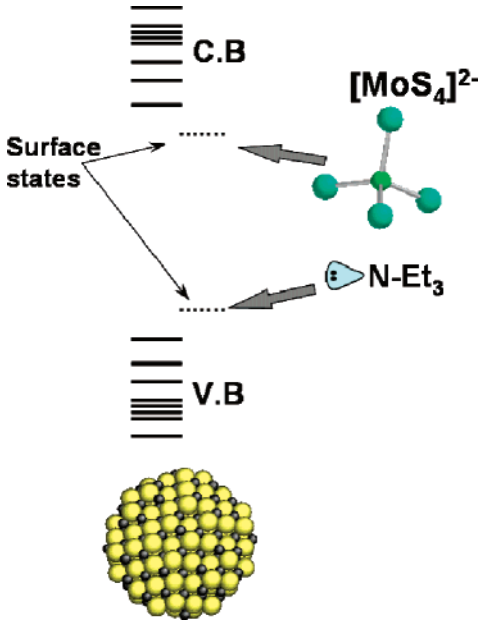

Figure 3. Qualitative energy orbital diagram for the interaction of naked RuS_2 NPs with $N(Et)_3$ and $[MoS_4]^{2-}$. VB and CB mean valence and conduction bands, respectively.[26]

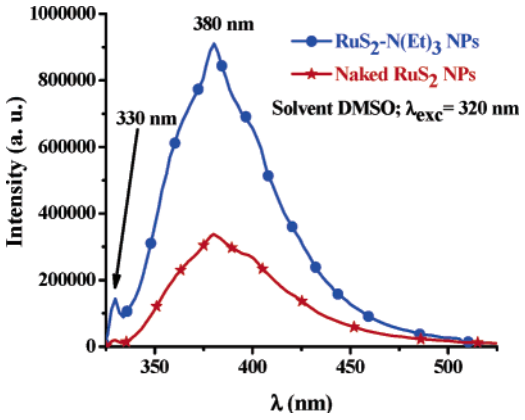

Figure 4. Fluorescence spectra of (1) naked RuS_2 and (2) $N(Et)_3$-capped RuS_2 colloidal DMSO dispersions. These dispersions were prepared as described in the Experimental Section.

mentioning that we have tested different Lewis bases as surface stabilizers; the base strength follows the sequence: $N(Et)_3$ (hard base) > DMSO (borderline base) > $[MoS_4]^{2-}$ (soft base). Therefore, a hard base with a well-localized electron lone pair (sp^3 orbital) increases not only the stability of the rather small RuS_2 NPs but also its fluorescence emission. The opposite is true for a soft base with eight electron pairs, type p, not so well oriented for overlapping with the Ru(II) empty d orbitals. The tetrathiomolybdate species can be bound through four different sites, in comparison with the amine ligand that can only coordinate to Ru through one nitrogen atom. Tetrathiomolybdate can also occupy S vacancies. The experimental evidences show that tetrathiomolybdate itself has a considerable UV−vis absorption without emission. This implies that emission of this anion is quenched through a radiationless process. Therefore the $[MoS_4]^{2-}$ species should be occupying empty surface states (see Figure 3) at the conduction band and quenching the fluorescence by a nonradiative recombination (charge transfer) from NPs excited states to $[MoS_4]^{2-}$ moiety.[27]

Whereas in the case of the DMSO molecule, it has an electron rich region S═O, where the sulfur has an electron lone pair

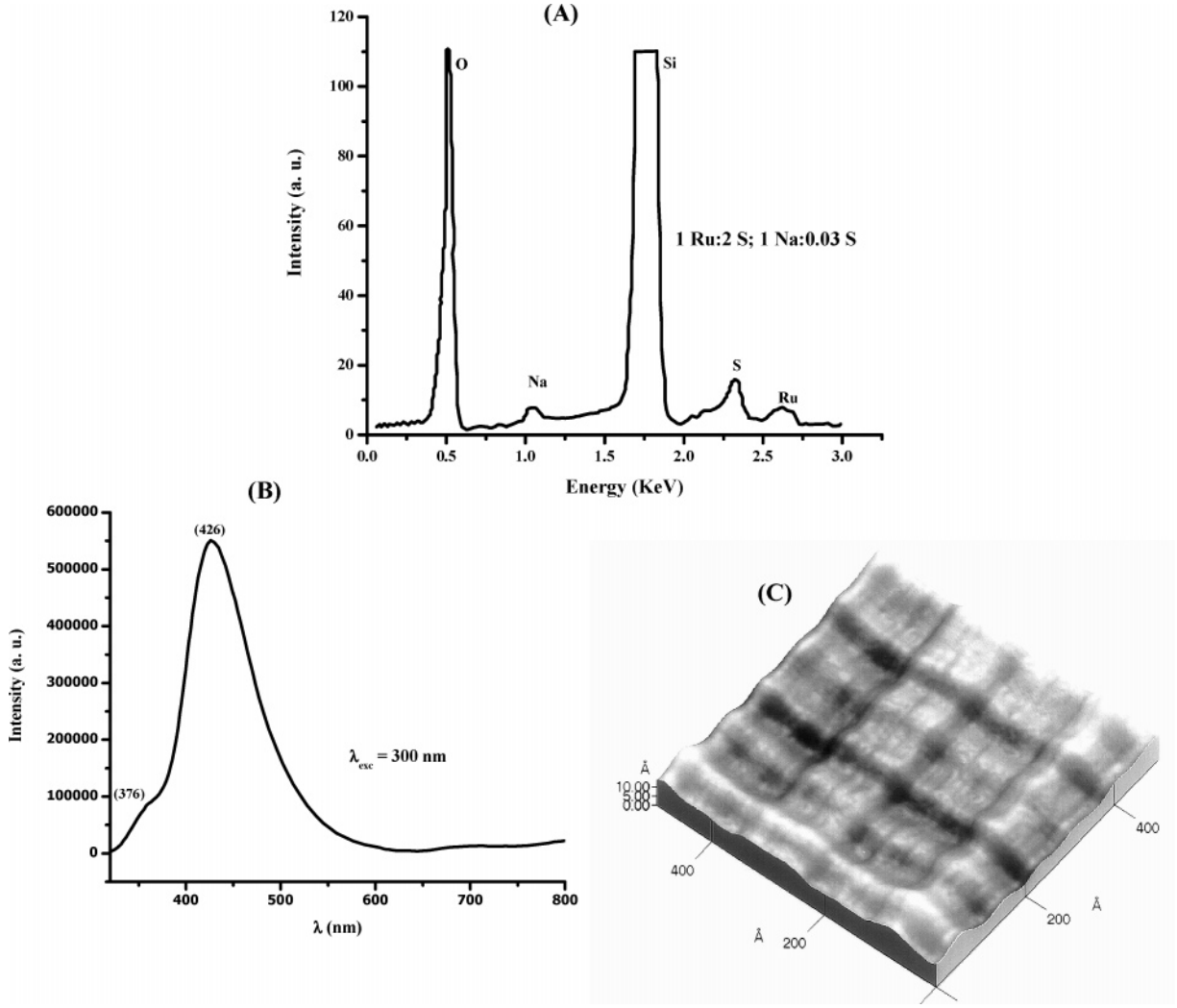

Figure 5. (A) Energy-loss dispersion spectrum of $N(Et)_3$ capped RuS_2 thin films. (B) Fluorescence spectrum of the same sample. (C) AFM topographic image of the same sample. The solid support in parts A and B was fused quartz wafer, while for (C) it was the (111) epitaxially grown silicon wafer.

and the oxygen has two lone pairs. The chemical affinity of the donor atoms toward Ru(II) is: S > N > O.

Thin Films. They were prepared as described in the Experimental Section. The thin films were characterized by EDS, powder X-ray diffraction spectroscopy, fluorescence spectroscopy, and AFM microscopy, Figure 5. The thickness of the films employed for ED, X-ray, and fluorescence spectroscopies was approximately 5 μm, to be appropriately detected by the first two spectroscopies.

The fluorescence spectrum of the $N(Et)_3-RuS_2$ nanostructured thin film shows a maximum emission at 426 nm, the spectrum is 275 nm wide, and the exitonic shoulder appears at 376 nm. Even though the irradiation wavelength is not exactly the same that of the colloid dispersion, we can observe that the thin film general profile spectrum changes. For the thin film spectrum, the shoulders are no longer present and the exitonic emission is unsharpened and low. The intensity of the emission is 1.6 times lower than for the colloid. We can impute the above-described changes and the red shift of the maximum emission band effect to particle agglomeration. As was stated in the Optical Properties section, $[MoS_4]^{2-}$ completely quenches the RuS_2 thin film fluorescence.

ED spectrum shows several peaks indicating the presence of oxygen, ruthenium, silicon, sodium, and sulfur. The corresponding stoichiometric proportions are displayed in Figure 5A. Silicon and oxygen can be accounted by the wafer, as well as part of the sodium. The remaining sodium comes from sodium sulfide used for the NPs synthesis, the slight sulfur excess may be due to unreacted Na_2S. Therefore, the chemical composition of the thin film sample corresponds to RuS_2. The AFM image shows a regular pattern, of a very thin film (1 nm of thickness). This pattern is probably a copy of the shape of the solid support ((111) epitaxially grown silicon wafer). On the other hand, the equivalent image for the $[MoS_4]^{2-}$-capped RuS_2 thin films does not show this regular pattern; this capping agent covers the whole surface and even more multilayers of tetrathiomolybdate are formed, Figure 6B. It is important to point out that these surface modified NPs have a wide size distribution and larger particle average diameter. Therefore, we consider that this is the reason for the change in behavior in comparison with the $N(Et)_3-RuS_2$ NPs. Regarding the $[MoS_4]^{2-}$-capped RuS_2 thin film ED spectrum, again we observe the presence of Si and O from the solid support, also it shows the presence of Ru, S, and Mo with the stoichiometric ratio displayed in Figure 6A. As observed, there is a large excess of $[MoS_4]^{2-}$, forming irregular layers on top of the RuS_2 NPs.

These thin films were also characterized by powder X-ray diffraction. We found that the naked $N(Et)_3$ and $RuS_2-[MoS_4]^{-2}$ thin films show a broad band corresponding to the (111) plane centered at 27.5°.

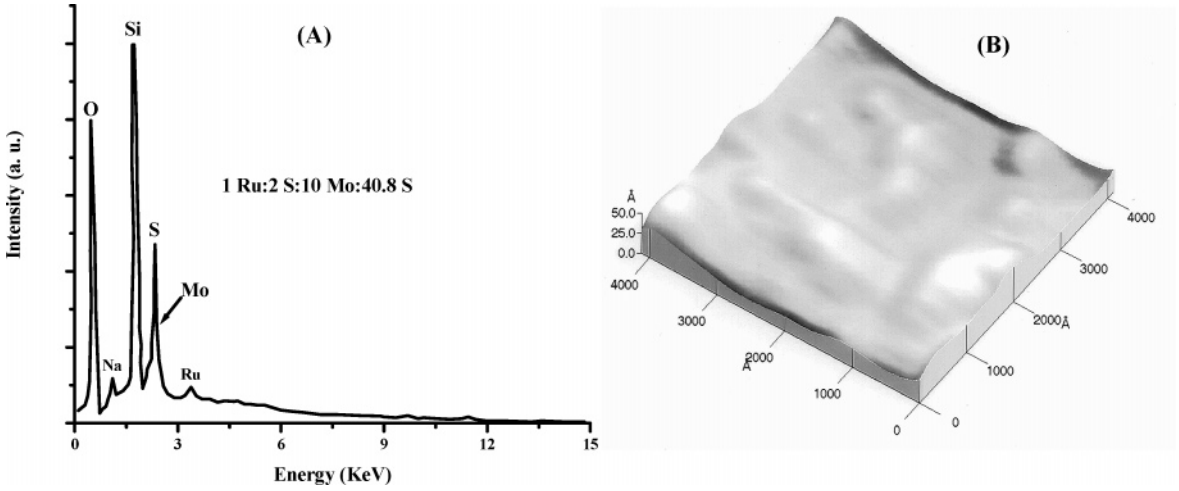

Figure 6. (A) Energy-loss dispersion spectrum of $[MoS_4]^{2-}$-capped RuS_2 thin films prepared over fused quartz wafers. (B) AFM topographic image of the same sample.

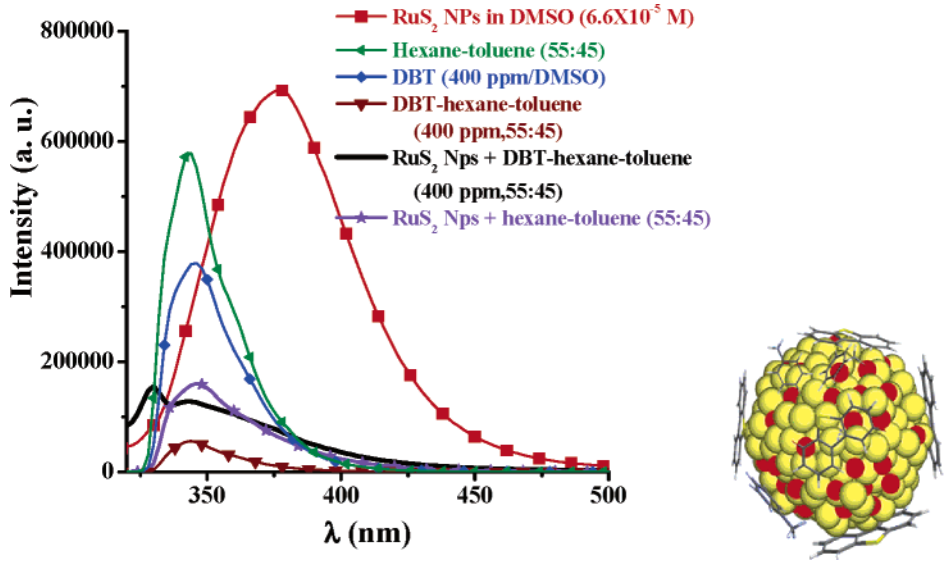

Figure 7. Fluorescence spectra of RuS_2 colloidal dispersion, components of the chemical mixture with composition similar to gasoline and the polar fractions of the resulting interactions, $\lambda_{excitation} = 300$ nm and room temperature. The corresponding concentrations are indicated in the insert of each spectrum. The image at the right shows a model of an average size NP interacting with dibenzothiophene (Bz_2S) and toluene molecules.

Naked and $RuS_2-[MoS_4]^{2-}$ thin films also display a small broad peak corresponding to the (211) plane centered at 39.31°, Figure S1, Supporting Information. These peaks correspond to the RuS_2 (laurite phase) diffraction pattern.[28]

RuS_2 NPs Interactions with a Fuel Model. In the literature there are several reports dealing with thiophene and dibenzothiophene interactions with ruthenium-based catalysts; however, only in two of them the interaction of nanoparticles with the previous two sulfur-containing compounds.[17e,29] We selected a fuel model for this study as already reported in the literature.[30] The main purpose of these experiments is to evaluate RuS_2 nanoparticles capacity to bind sulfur-containing aromatic compounds. The mixture of the fuel model with the colloidal dispersion yielded a two-phase reaction system. Both phases were analyzed, and it is important to point out that all chemical changes take place in the polar phase, i.e., DMSO portion. These changes were monitored by UV−vis absorption and emission spectroscopies. The fluorescence spectra are more illustrative of these changes since the absorption spectra show very wide overlapping bands. The results of some experiments in which we studied the interaction of RuS_2 NPs with toluene−hexane, Bz_2S, and Bz_2S toluene−hexane are shown in Figure 7. It is in general observed the quenching of the fluorescence of the fluorophoric species, RuS_2, by toluene and Bz_2S when they interact. On the green-line spectrum, the quenching of the fluorescence is due to the three following interactions: Bz_2S-Bz_2S, toluene−toluene, and Bz_2S−toluene, all of them are the well-known π interactions. The orange line only is indicative of the interaction between RuS_2 and toluene; there is not complete quenching of the fluorescence due to the very low concentration of the ruthenium sulfide NPs. Finally, the black line shows the interaction of the NPs with the fuel components model; here at least five interactions take place: Bz_2S-Bz_2S, toluene−toluene, Bz_2S−toluene, RuS_2-Bz_2S, and RuS_2−toluene. The latter two are displayed in the interaction model, Figure 7; where the π molecular orbitals of the aromatic rings interact with the surface of the NPs. Again, remaining fluorescence is observed due to the low concentration of the RuS_2 nanoparticles. These experiments clearly show the great chemical affinity of Ru_2S nanoparticles toward aromatic rings present in crude oil. Research is in progress in our laboratory.

In summary, this is a simple colloidal system that clearly demonstrates the strong interaction of RuS_2 NPs with dibenzothiophene and toluene, under mild reaction conditions, strongly

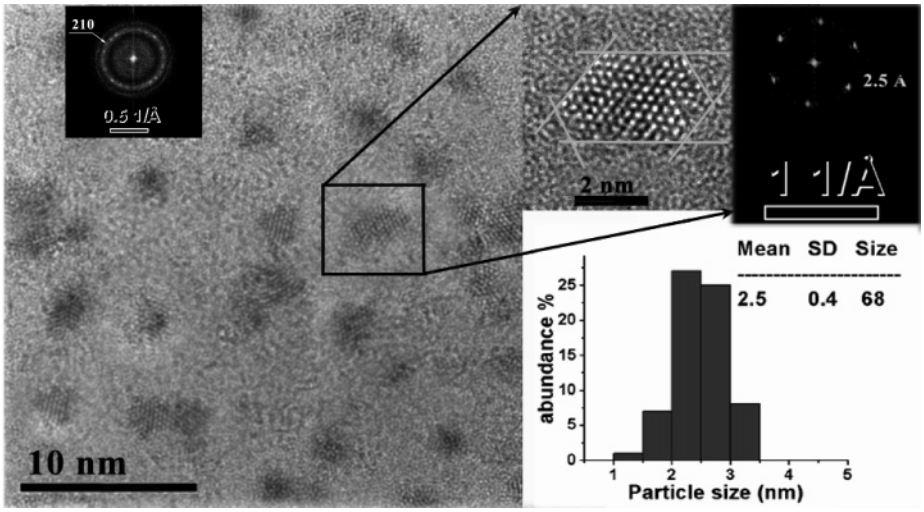

Figure 8. HR-TEM micrograph of naked RuS_2 nanoparticles (after 30 days) prepared from $RuCl_3.nH_2O$ (2×10^{-4} M) and Na_2S (4×10^{-4} M) in DMSO. The corresponding particle size distribution histogram of naked-RuS_2 nanoparticles is shown.

TABLE 1: Estimated Dispersion Characteristics from HR-TEM Particle Size Distribution Data

clusters concentration (particles/mL)	total surface [m^2]	specific surface [m^2/g]	(surface/volume) ratio [m^{-1}]	percentage of atoms at the surface
7.5×10^{14}	6×10^{-1}	363.2	2.5×10^9	62.5

suggesting the possibility of its use as catalyst in hydrodesulfurization processes.

Structural and Morphological Analysis. A HR-TEM study was carried out after one month of preparation of the colloidal dispersion. This guarantees the stability of the dispersion and consequently the reproducibility of the results since only slight modification in particle size and sizes distribution are expected under these conditions.

Ruthenium chalcogenide belongs to the family of transition metal disulfides crystallizing in the pyrite structure (space group *Pa*3, $a = 0.56095$ nm, with Ru^{2+} in 4(a) and S_2^- in 8(c) positions, and $x = 0.3879$).[31] The structure is formed by three-dimensional corner shared RuS_{12} octahedrons.

Figure 8 shows a selected HR-TEM image of RuS_2 naked nanocrystallites. The measured reflections agree with the reported values for pyrite type (cubic) structure of the stable RuS_2 macrocrystalline phase. The particle size distribution plot shows a narrow distribution with mean diameter of 2.5 nm, and a standard deviation of ± 0.4 nm. Table 1 summarizes the properties of the RuS_2-naked nanoparticles, calculated assuming spherical particles and taking into account the structure parameters ($a = 0.56095$ nm, 4 molecules/cell).

Fast Fourier transform (FFT) images obtained from multiple (naked RuS_2) nanoparticles image processing show preferential exposed planes along (210), first ring in the FFT in Figure 8. The {111} planes had been reported as the most common and reactive exposed faces in RuS_2.[17d,e,32] A closer view of one of the NPs shows a RuS_2 naked nanocrystal oriented at [111] direction, this is corroborated with the corresponding FFT.

The structural properties of RuS_2 and the interactions of the naked NPs with the solvent and the surface modifiers are responsible for its crystalline habit modification. RuS_2 nanocrystals tend to be exposed toward the surface at the (111) and (210) planes, Figures 8 and S1 (the corresponding X-ray diffraction patterns, see Supporting Information). From the crystallographic point of view, the {111} and {002} family planes are composed by Ru atoms while the {210} family planes are formed by Ru and S atoms. Therefore the first two family planes contain a large amount of exposed Ru^{2+} ions, that exhibit Lewis-acid character and therefore tend to minimize their surface energies by attaching Lewis bases (e.g., DMSO and/or capping agent molecules). Surface modification of RuS_2 NPs favors the development of the {210} family planes, during the nanocrystals growth process.

The X-ray diffraction patterns (Figure S1, Supporting Information) of deposited samples are very similar for naked RuS_2 and $RuS_2-[MoS_4]^{2-}$. In all cases it can be observed widespread peaks over the range of the main reflections expected for RuS_2 in pyrite-like structure. However, these broad peaks, which resulted from the very small particles sizes, are not sufficient and clear evidence to state that the patterns unambiguously correspond to the RuS_2 phase.

For the $RuS_2-[MoS_4]^{2-}$ sample, HR-TEM micrographs also show preferred nanocrystallite orientation along the [001] zone axis (square array in the FFT, Figure 9), while $RuS_2-N(Et)_3$ micrograph shows nanocrystallites with several different planes (023), (311), and (222). These different orientations compared with those of naked nanoparticles suggest that both capping agents modify in different forms; the association−dissociation equilibrium at the nanoparticles surface in turn modifies the nanocrystals surface planes.

Right image of Figure 9 shows an ordered matrix overlapping with the $RuS_2-[MoS_4]^{2-}$ NPs lattice.

Taking into account this underlying matrix, we decided to accomplish a deep structural study of the $RuS_2-[MoS_4]^{-2}$ sample. Z contrast image technique shows the presence of an ordered matrix, possibly MoO_3, in which RuS_2 NPs are embedded. This is corroborated by the profile of the zone showed in Figure 10b. Here the profile suggests the presence of a MoO_3 crystalline phase, as previously reported.[33] The HR-TEM study supports these results, where the images were processed with the Digital Micrograph software. The crystalline planes shown in Figure 10c) correspond to the interplanar distance 0.359 nm. This lattice matches very well with that of MoO_3 monoclinic phase in the planes (200).[34] However, in Figure 10d), some isolated RuS_2 nanoparticles exhibit reflections of 0.25 and 0.18 nm which correspond to the (210) and (221) planes of cubic phase.

To complete the characterization of the isolated RuS_2 NPs, an EELS spectrum was obtained using the diffraction mode on

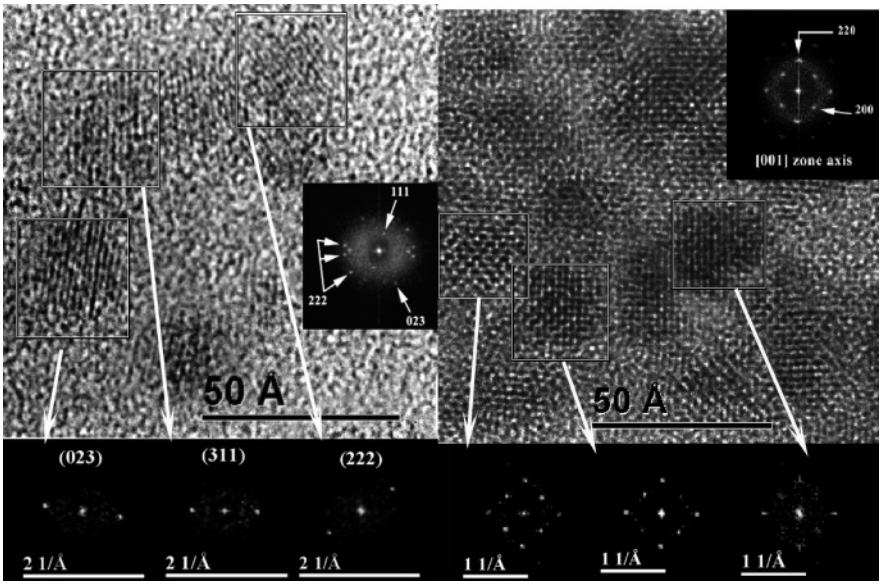

Figure 9. Selected HR-TEM micrographs of $RuS_2-N(Et)_3$ and $RuS_2-[MoS_4]^{2-}$ (right image) nanoparticles, prepared from the interaction of pre-prepared RuS_2 nanoparticles in DMSO with 1.4×10^{-3} and 1×10^{-3} M DMSO solutions of $N(Et)_3$ and $(NH_4)_2MoS_4$, respectively. In addition to the global FFT of each micrograph, the FFT of selected particles are shown in the lower part of each micrograph.

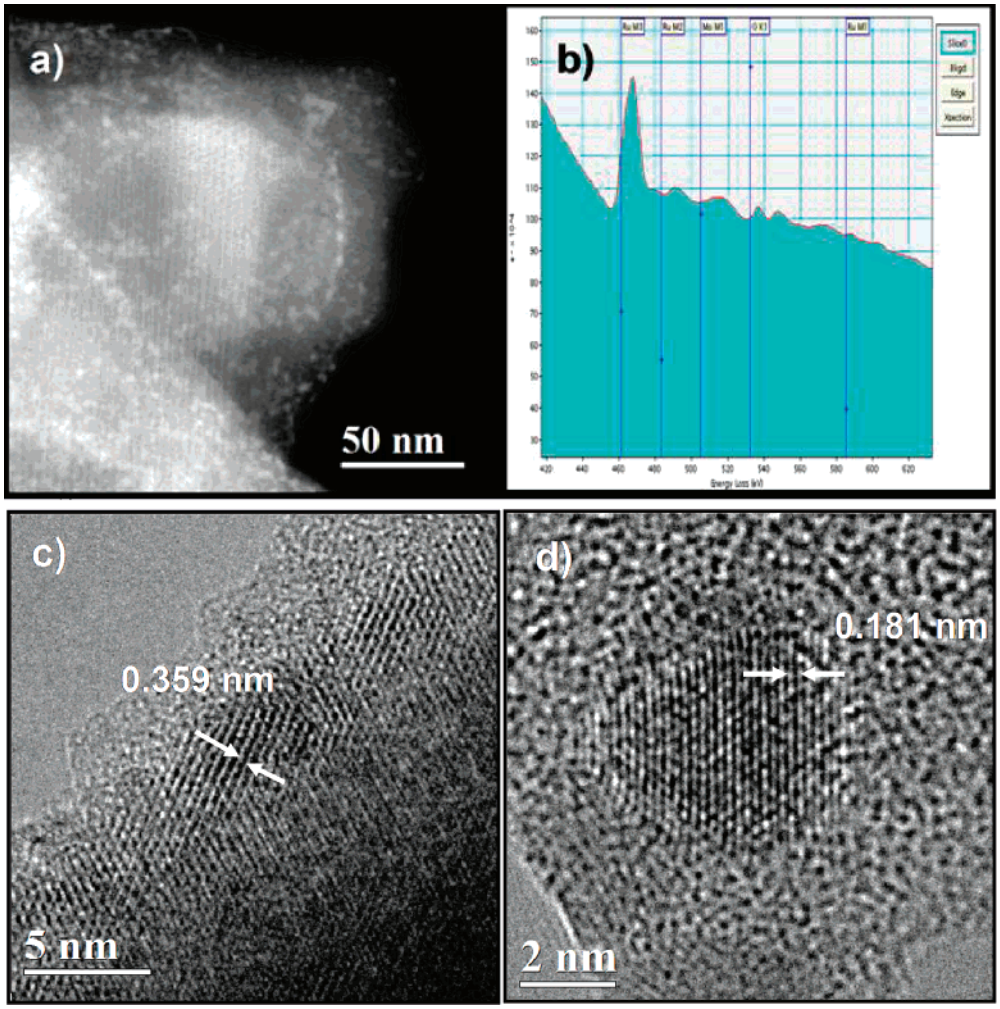

Figure 10. (a) HAADF image from a general zone of RuS_2 NPs embedded in to a crystalline matrix. (b) EELS spectrum from the zone illustrated in (a). (c) Conventional HR-TEM shows a crystalline matrix whose interplanar distance corresponds to the (200) reflection of monoclinic MoO_3. (d) Small nanoparticles between 2 and 5 nm with lattice fringes of 0.181 nm. This reflection corresponds to the (221) reflection of RuS_2.

a zone constituted by nanoparticles exclusively, parts a and b of Figure 11. The profile in this case corresponds to S (S−L1 229 eV) and Ru (Ru−M2 483 eV). In this particular case we do not have evidence of the presence of either Mo or O.[35] Research is in progress to fully determine the origin of the of the MoO_3 ordered matrix.

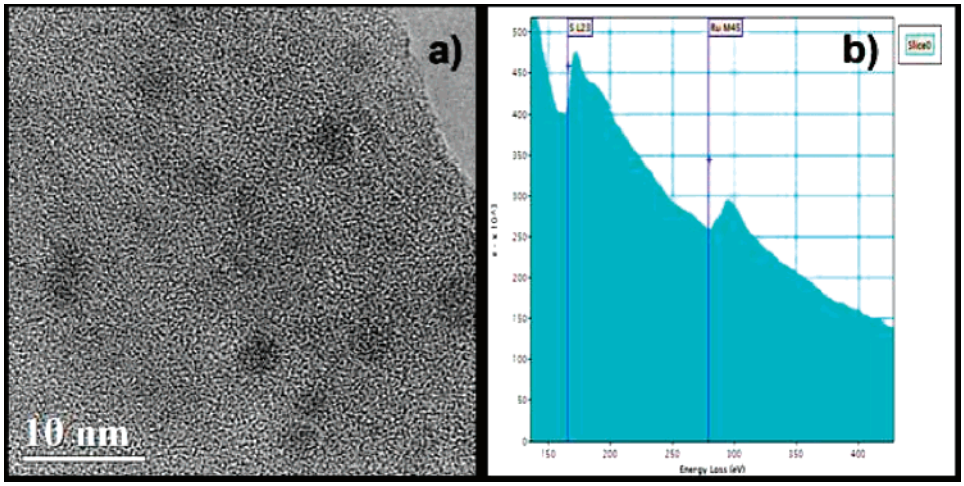

Figure 11. (a) Conventional HR-TEM image of some isolated RuS_2 NPs and (b) EELS spectrum from the zone illustrated in a, obtained in diffraction mode. The profile corresponds to the RuS_2 laurite phase.

Concluding Remarks

We found a novel, simple, and inexpensive method of RuS_2 NPs synthesis in colloidal DMSO dispersions, under mild reaction conditions. These colloidal RuS_2 dispersions are stable during several months and any flocculation or red shift was not observed with time. In a typical RuS_2 colloidal dispersion, the percentage of atoms exposed in the surface, is approximately 63%.

Under normal reaction conditions, RuS_2 has only one solid phase; as CdSe, ruthenium sulfide is an extraordinary fluorescent material. Then, this opens the possibility to use nanostructured RuS_2 in photonic devices and also for biological labeling.

RuS_2 NPs are able to present interactions of different strength with several Lewis bases, such as $N(Et)_3$, $[MoS_4]^{2-}$, toluene, dibenzothiophene, and DMSO. While hard bases increase the fluorescence intensity of RuS_2 NPs, soft bases quench it. As a result, we have a simple colloidal system that clearly demonstrates the strong interaction of RuS_2 NPs with dibenzothiophene and toluene, the components of the chemical mixture with composition similar to gasoline, under room reaction conditions. This is achieved by monitoring the reaction system with an inexpensive and common spectroscopic method. As consequence, it is possible to use RuS_2 colloids as a catalyst in the hydrodesulfurization process. Research is in progress to determine the catalytic role of the colloidal RuS_2 nanoparticles.

RuS_2 NPs thin films were deposited over fused quartz wafers, characterizing them completely by X-ray diffraction, scanning electron microscopy, EDS, HR-TEM, AFM, and fluorescence. $RuS_2-N(Et)_3$ NPs are used to obtain thin films of particle very regular arrangements, while when $RuS_2-[MoS_4]^{2-}$ NPs were used, it was observed that the tetrathiomolybdate totally covers the thin films. In this case, a particle growth is observed in the preferential plane (211).

HR-TEM results also show that dispersions of RuS_2 naked nanoparticles have a narrow particle size distribution centered at 2.4 nm (standard deviation $= \pm 0.4$ nm), whereas the use of capping agents as $N(Et)_3$ and $(NH_4)_2MoS_4$ does not appreciably modify the RuS_2 particle size. It was also observed that the use of different capping agents modifies in different manner the morphology of the NPs. In the case of $RuS_2-[MoS_4]^{2-}$, some of the nanoparticles are immersed in a crystalline matrix of MoO_3, supported by the evidence of HR-TEM, HAADF, and EELS studies. Additionally, EELS studies confirm the fact that the isolated nanoparticles are RuS_2 cubic phase species.

Acknowledgment. We acknowledge financial support from Projects IN100398, IN105102-2, and IN110405 PAPIIT-DGAPA-UNAM and CONACyT-SEP E-43662-F. We thank Dr. Carlos Vazquez Lopez (CINVESTAV, D. F.) for obtaining the AFM images.

Supporting Information Available: X-ray diffraction patterns of capped (MoS_4^{2-}, Et_3N) and naked RuS_2 nanoparticles, electronic absorption spectra of the reaction mixture of a RuS_2 colloidal dispersion in DMSO with $(NH_4)_2MoS_4$ in a 1:10 molar ratio at room temperature, at several times, electronic absorption spectrum of $(NH_4)_2MoS_4$ in DMSO at room temperature, and electronic absorption spectra of the reaction mixture of a RuS_2 colloidal dispersion in DMSO with $N(Et)_3$ in a 1:14 molar ratio at room temperature, at several times. This material is available free of charge via the Internet at http://pubs.acs.org.

References and Notes

(1) (a) Le Nagard, N.; Bouanani, A.; Ezzaouia, H.; Gorochov, O. *J. Cryst. Growth* **1990**, *104*, 365. (b) Sutarno, O.; Knop, O.; Reid, K. I. G. *Can. J. Chem.* **1967**, *45*, 1391.

(2) (a) Lee, M. C.; Huang, C. R.; Watson, Yang, T. J. *Solid State Comm.* **1989**, *71*, 899. (b) Lin, S. S.; Huang, Y. S. *Solid State Comm.* **1989**, *69*, 589.

(3) Collel, H.; Bronold, M.; Fiechter, S.; Tributsch, H. *Surface Sci. Lett.* **1994**, *303*, L361.

(4) Huang, J. K.; Huang, Y. S.; Yang, T. R. *J. Phys. Condens. Matter*. **1995**, *7*, 4175, and references therein.

(5) Tributsh, H. Metal sulfides in photovoltaic, photoelectrochemical and solar biological energy conversion. In *Sulfur. Its significance for chemistry, for geo-, bio-, and cosmosphere and technology;* Müller, A., Krebs, B., Eds.; Studies in Inorganic Chemistry 5; Elsevier: Amsterdam, 1984; pp 277−310.

(6) Sassani, D. C.; Shock, E. L. *Geochim. Cosmochim. Acta* **1998**, *62*, 2643.

(7) Sedon, E.; Sedon, K. The Chemistry of Ruthenium. In *Topics in Inorganic and General Chemistry*; Elsevier: Amsterdam, 1984; pp 159−160.

(8) (a) Passareti, J. D.; Dwight, K.; Wold, A.; Croft, W. J.; Chianelli, R. R. *Inorg. Chem.* **1981**, *20*, 2631. (b) Kelty, S. P.; Li, J.; Chen, J. G.; Chianelli, R. R.; Ren, J.; Whangbo, M.-H. *J. Phys. Chem. B* **1999**, *103*, 4649.

(9) Berhault, G.; Lacroix, M.; Breysse, M.; Maugé, F.; Lavalley, J.-C.; Qu, L. *J. Catal.* **1997**, *170*, 37.

(10) (a) Chaparro, A. M.; Alonso-Vante, N.; Salvador, P.; Tributsch, H. *J. Electrochem. Soc.* **1997**, *144*, 2991. (b) Hara, K.; Sayama, K.; Arakawa, H. *Chem. Lett.* **1998**, 387.

(11) (a) Lacroix, M.; Boutarfa, N.; Guillard, C.; Vrinat, M.; Breysse, M. *J. Catal.* **1989**, *120*, 473. (b) Harvey, T. G.; Matheson, T. W. *J. Catal.* **1986**, *101*, 253.

(12) Heise, W. H.; Lu, K.; Kuo, Y.-J.; Udovic, T. J.; Rush, J. J.; Tatarchuk, B. J. *J. Phys. Chem.* **1988**, *92*, 5184.

(13) Jobic, H.; Clugnet, G.; Lacroix, M.; Yuan, S.; Mirodatos, C.; Breysse, M. *J. Am. Chem. Soc*. **1993**, *115*, 3654.

(14) (a) Lacroix, M.; Yuan, S.; Breysse, M.; Dorémieux-Morin, C.; Fraissard, J. *J. Catal*. **1992**, *138*, 409. (b) Isoda, T.; Nagao, S.; Ma, X.; Korai, Y.; Mochida, I. *Energy Fuels* **1996**, *10*, 487. (c) Gwaunza, M.; Adesina, A. *React. Kinet. Catal. Lett*. **1997**, *62*, 55.

(15) (a) Smelyansky, V.; Hafner, J.; Kreese, G. *Phys. Rev. B* **1998**, *58*, R1782. (b) Tan, A.; Harris, S. *Inorg. Chem.* **1998**, *37*, 2215.

(16) (a) Aray, Y.; Rodríguez, J. *Chem. Phys. Chem*. **2001**, 599. (b) Aray, Y.; Rodríguez J.; Vega, D.; Coll, S.; Rodríguez-Arias, N. E.; Rodríguez, F. *J. Phys. Chem. B* **2002**, *106*, 13242.

(17) (a) Ashokkumar, M.; Kudo A.; Sakata, T. *J. Mater. Sci*. **1995**, *30*, 2759. (b) Moraweck, B.; Bergeret, G.; Cattenot, M.; Kougionas, V.; Geantet, C.; Portefaix, J.-L.; Zotin, J.-L.; Breysse, M. *J. Catal*. **1997**, *165*, 45. (c) Hirai, T.; Nomura, Y.; Komasawa, I. *J. Nanoparticle Res*. **2003**, *5*, 61. (d) Aouine, M.; Geanet, C.; Epicier, T. *Catal. Today* **2001**, *66*, 87. (e) Cai, T.; Song, Z.; Rodríguez, J. A.; Hrbek, J. *J. Am. Chem. Soc.* **2004**, *126*, 8886.

(18) Froment, P.; Genet, M. J.; Devillers, M. *J. Electron Spectrosc. Relat. Phenom.* **1999**, *104*, 119.

(19) Prabhi, K. R.; Devan, N.; Chandrasekaran, S. *Synlett* **2002**, 1762.

(20) Wu, Li-M.; Seo, D.-K. *J. Am. Chem. Soc*. **2004**, *126*, 4676.

(21) Hulliger, F. *Nature* **1963**, *200*, 1064.

(22) Calligaris, M.; Carugo, O. *Coord. Chem. Rev.* **1996**, *153*, 83.

(23) Reichardt, C. *Solvents and Solvent Effects in Organic Chemistry*, 2nd ed.; VCH: New York, 1990.

(24) Cullis, C. F.; Hopton, J. D.; Swan, C. J.; Trim, D. L. *J. Appl. Chem.* **1968**, *18*, 335.

(25) (a) Brus, L. E. *J Chem Phys.* **1983**, *79*, 5566. (b) Brus, L. E. *J. Chem. Phys.* **1984**, *80*, 4403. (c) Brus, L. E. *J. Phys. Chem.* **1986**, *90*, 2555. (d) Nedeljkovic, J. M.; Patel, R. C.; Kaufman, P.; Joyce-Pruden, C.; O'Leary, N. *J. Chem. Educ*. **1993**, *70*, 342.

(26) Fiechter, S. *Sol. Energy Mater. Sol. Cells*. **2004**, *83*, 459.

(27) (a) Zhang, J. Z. *J. Phys. Chem. B* **2000**, *104*, 7239. (b) Lakowicz, J. R. *Principles of Fluorescence Spectroscopy*, 2nd ed.; Kluwer Academic/Plenum: New York, 1999.

(28) JCPDS-ICDD. PCPDFWIN version 2.2, 2001, PDF#800669 card.

(29) Raje, A. P.; Liaw, S.-J.; Srinivasan, R.; Davis, B. H. *Appl. Catal., A* **1997**, *150*, 297.

(30) McKindly, S. G.; Vecchi, P.; A. Ellern, A.; Angelici, R. J. *Dalton Trans.* **2004**, 788.

(31) Lutz, H. D.; Muller, B.; Schmidt, Th.; Stingl, Th. *Acta Crystallogr. C* **1990**, *46*, 2003.

(32) Huang, Y. S.; Chen, Y. F. *Phys. Rev. B* **1988**, *38*, 7997.

(33) Ahn, C. C.; Krivanek, O. L.; Burgner, R. P.; Disko, M. M.; Swann, P. R. *EELS Atlas. A Reference Collection of Electron Energy Loss Spectra Covering all Stable Elements*; Gatan Incorporated and HREM Facility, Arizona State University: Tempe, AZ, 1983.

(34) JCPDS-ICDD. PCPDFWIN version 2.2, 2001, PDF #891554 card.